Probing exciton dynamics using Raman resonances in femtosecond x-ray four-wave mixing

Satoshi Tanaka[1,*] and Shaul Mukamel[2,3,†]
[1]*CIAS, Osaka Prefecture University, Sakai 599-8531, Japan*
[2]*Department of Chemistry, University of Rochester, Rochester, New York 14627*
[3]*Department of Physics and Astronomy, University of Rochester, Rochester, New York 14627*
(Received 6 November 2002; published 28 March 2003)

Time-resolved coherent x-ray Raman signals of molecules are computed by formulating the nonlinear response in terms of correlation functions of charge and current densities. Simulations performed on one-dimensional molecular chains demonstrate that Raman resonances provide a direct local probe for valence-excitation dynamics with high spatial and temporal resolutions.

DOI: 10.1103/PhysRevA.67.033818 PACS number(s): 42.65.Dr, 33.20.Rm

I. INTRODUCTION

Recent rapid progress in the development of coherent ultrafast x-ray pulses opens up a new era in x-ray spectroscopy [1–6]. As pulse intensities and coherence properties are improved, nonlinear all x-ray spectroscopies should become feasible, allowing the direct investigation of electron motions in atoms, molecules, and solid-state materials in real space and real time. The high temporal (attosecond) and spatial (subnanometer) resolution of these techniques offers a new window into molecular structure and dynamical processes. Relaxation dynamics of optically excited states have been extensively studied by means of time-resolved x-ray-diffraction and -absorption techniques [7–10]. Wilson and co-workers have calculated time-resolved x-ray spectroscopies by a direct extension of the conventional theory of stationary x-ray-diffraction and -absorption [11,12].

Since the soft-x-ray wavelength ($1-10$ nm) is comparable to a molecular size, the dipole approximation which imposes strict selection rules in optical spectroscopy does not apply, allowing a bird's eye view of the entire manifold of electronic transitions and inducing a strong dependence of the signal on wave vectors [13]. The same state of affairs exists in vibrational spectroscopy where short-wavelegnth neutron scattering provides a global picture of the entire spectrum of modes, in contrast with optical Raman and infrared techniques which are restricted by the selection rules [14]. Nonlinear x-ray spectroscopies, thus, provide detailed information on spatial coherence in excited states. By tuning the x-ray frequencies across the core excitations of various atoms it may become possible to investigate in detail the nonlocal nature of valence-electronic excitations.

We have recently formulated a microscopic theory of nonlinear x-ray spectroscopy in terms of nonlinear response functions (NRF) [15], which in turn are given by combinations of multitime correlation functions of the current- and charge-density operators. It fully incorporates nonlocal effects in time and space and provides a systematic approach for computing the nonlinear response to any desired order in the incoming fields. The time evolution of the density matrix is represented by the *Liouville space pathways* for the nonlinear response which provide an intuitive picture of time-resolved spectroscopies. This Liouville space NRF formulation has several advantages over descriptions based upon the wave function in Hilbert space [16]: Time ordering of the interactions with the fields is properly maintained and dephasings effects between the different electronic states cannot be introduced in the wave function representation. A similar approach was subsequently used by Bratos *et al.* [17]. Application of this formulation to various nonlinear x-ray techniques [18–21] demonstrated how the spatial coherence of an excited electron and/or a valence exciton between different atomic sites may be directly investigated.

This paper focuses on Raman resonances in x-ray four-wave mixing. Four-wave mixing is an important family of third-order optical techniques involving the coherent interaction of the system with three incoming beams with wave vectors and frequencies $\mathbf{k}_1\omega_1$, $\mathbf{k}_2\omega_2$, and $\mathbf{k}_3\omega_3$, to generate a signal beam at various combinations of three wave vectors $\mathbf{k}_s=\pm\mathbf{k}_1\pm\mathbf{k}_2\pm\mathbf{k}_3$ and $\omega_s=\pm\omega_1\pm\omega_2\pm\omega_3$. Raman spectroscopy uses the difference of two high-frequency fields (ω_1,ω_2) to probe lower-frequency resonances $\omega_1-\omega_2=\omega_{ab}$. Traditionally, the Raman process is performed with optical fields which may be resonant with electronic transitions, and the Raman low-frequency resonances correspond to vibrational motions and low-lying electronic excitations [22]. The ordinary Raman process uses a single external field ω_1 and the signal ω_s is generated by spontaneous emission. This spontaneous Raman-scattering (SRS) technique falls within the realm of linear spectroscopy since the signal is proportional to the incident intensity. The advent of nonlinear spectroscopy in the 1960's opened many new avenues for detecting Raman resonances through differences of several incoming beams. Most common is coherent Raman spectroscopy (CRS). This is a third-order four-wave mixing process which generates a signal at $\mathbf{k}_s=\mathbf{k}_1-\mathbf{k}_2+\mathbf{k}_3$; $\omega_s=\omega_1-\omega_2+\omega_3$. The Raman resonances are observed when the signal is monitored vs $\omega_1-\omega_2$ [23]. Both SRS and CRS have been developed into powerful analytical and diagnostic tools for vibrational motions. In CRS the signal *fields* generated by all molecules add coherently, hence the strong directionality. In SRS, in contrast, there is no spatial coherence between mol-

*Electronic address: stanaka@ms.cias.osakafu-u.ac.jp;
URL: http://ms.cias.osakafu-u.ac.jp/ stanaka/My_homepage.html
†Electronic address: mukamel@chem.rochester.edu;
URL: http://mukamel.chem.rochester.edu

ecules and the signal *intensities* of various molecules are added.

Analogous processes can be studied in the x-ray regime. Here, the high-frequency beams create core-hole excitations and the low-frequency transitions being probed are optical valence excitations. Thanks to the development of synchrotron x-ray sources, many spontaneous x-ray Raman-scattering (SXRS) studies have been carried out on molecules and solid materials [24–28]. However, the coherent analog, CXRS, discussed in Refs. [19,21], has not been reported yet. In our previous papers, we calculated time-resolved spontaneous [20] and the stationary coherent x-ray Raman-scattering spectra [19] and showed how these techniques may be used to probe relaxation dynamics of valence-exciton states. Simulations of the stationary CXRS response in a one-dimensional molecular chain [19] have shown that the spatial coherence of valence exciton can be precisely monitored by tuning the x-ray frequencies to different atomic core resonances. Thus, the wave vector and frequency profiles of CXRS carry most valuable dynamical information on energy and charge-transfer processes.

The aim of this paper is to develop the theory for time-resolved coherent x-ray Raman scattering (TCXRS) and demonstrate its potential utility as a universal local probe that can readily detect real-time dynamics of valence excitations in molecules. This four-wave-mixing process uses two time-coincident pulses $\mathbf{k}_1$ and $\mathbf{k}_2$, and the x-ray signal at $\mathbf{k}_s=\mathbf{k}_1-\mathbf{k}_2+\mathbf{k}_3$ is detected as a function of the variable delay of a third $\mathbf{k}_3$ beam with respect to $\mathbf{k}_1$ and $\mathbf{k}_2$. We adopt the same molecular model chain used in our previous study [19]. Investigating real-time relaxation dynamics of optically excited states allows to probe exciton transport and trace the origin of their strong nonlinear response to optical fields.

We present the model in Sec. II and develop a closed expression for the time-resolved CXRS in Sec. III. Details of the derivations are given in the Appendices. Numerical simulations are given in Sec. IV, and the results are finally discussed in Sec. V.

II. THE MODEL

We consider a molecular chain with $N=8$ atoms, each having three (core, occupied valence, and unoccupied conduction) orbitals, as shown in Fig. 1(a) [19]. This can be regarded as a model for many types of conjugated molecules such as polydiacetylene, polyacetylene and β-carotenoids [29,30] and halogen bridged mixed valence platinum compounds [31–33]. We include the transfer of the conduction electron (t_c) and valence hole (t_v), but neglect core hole transfer. On-site attractive Coulomb interactions between a core hole and a conduction electron (core-exciton effect) (U_{ac}), between the valence hole and a conduction electron (valence-exciton effect) (U_{vc}), and the on-site repulsive Coulomb interaction between conduction electrons (U_{cc}) are taken into account, in addition to the Coulomb repulsion between core holes (U_{aa}). Since states with two valence holes do not contribute to the CXRS process, we did not include the Coulomb repulsion between valence holes.

The single-electron picture of the valence excitations of this molecule is depicted in Fig. 1(a) along with the interaction and energy parameters for all sites. The zero orbital energy is taken at the midgap between the valence and conduction levels. For clarity, the orbitals for the intermediate sites are not drawn.

The molecular model Hamiltonian H_m is thus given by

$$\begin{aligned}\hat{H}_m=&-\sum_{l=1,\sigma}^{N}\epsilon_a a_{l\sigma}^{\dagger}a_{l\sigma}+\sum_{l=1,\sigma}^{N}\epsilon_v v_{l\sigma}^{\dagger}v_{l\sigma}-\sum_{l=1,\sigma}^{N}\epsilon_c c_{l\sigma}^{\dagger}c_{l\sigma}\\&+\sum_{l,m=1,\sigma,l\neq m}^{N}t_{v:lm}v_{l\sigma}^{\dagger}v_{m\sigma}+\sum_{l,m=1,\sigma,l\neq m}^{N}t_{c:lm}c_{l\sigma}^{\dagger}c_{m\sigma}\\&-\sum_{l=1,\sigma,\underline{\sigma}}^{N}U_{ca}c_{l\sigma}^{\dagger}c_{l\sigma}(1-a_{l\underline{\sigma}}^{\dagger}a_{l\underline{\sigma}})-\sum_{l=1,\sigma,\underline{\sigma}}^{N}U_{cv}c_{l\sigma}^{\dagger}c_{l\sigma}\\&\times(1-v_{l\underline{\sigma}}^{\dagger}v_{l\underline{\sigma}}),\end{aligned}\tag{1}$$

where l and σ denotes the site and the spin indices, and $a_{l\sigma}$ ($a_{l\sigma}^{\dagger}$), $v_{l\sigma}$ ($v_{l\sigma}^{\dagger}$), and $c_{l\sigma}$ ($c_{l\sigma}^{\dagger}$) are the electron annihilation (creation) operators for the core, valence, and conduction orbitals, respectively. $t_{v:lm}$ ($t_{c:lm}$) are transfer integrals between the valence (conduction) orbitals. Transfer integrals between core orbitals are neglected because they are usually very small (much smaller than 0.1 eV) due to very weak overlaps of the highly localized core orbitals [34]. The Coulomb interactions between the core hole and the conduction electrons, and between a valence hole and a conduction electron are denoted U_{ca} and U_{cv}, respectively.

The eigenstates of H_m were computed by direct diagonalization of the 81×81 matrix using the following basis set for the single-core excited states:

$$|\underline{a};l\rangle_e=\frac{1}{2}(a_{1\uparrow}c_{l\uparrow}^{\dagger}+a_{1\downarrow}c_{l\downarrow}^{\dagger})|g\rangle,\tag{2a}$$

$$|\underline{b};l\rangle_e=\frac{1}{2}(a_{N\uparrow}c_{l\uparrow}^{\dagger}+a_{N\downarrow}c_{l\downarrow}^{\dagger})|g\rangle,\tag{2b}$$

with $l=1,\ldots,N$, where $\underline{j}$ ($j=a,b$) denotes a core hole located at site a or b, and $|g\rangle$ denotes the ground-state configuration,

$$|g\rangle=\prod_{l=1,\sigma}^{N}a_{l\sigma}^{\dagger}v_{l\sigma}^{\dagger}|\mathrm{vac}\rangle,\tag{3}$$

where $|\mathrm{vac}\rangle$ is the vacuum state (no electrons). For the valence-exciton states, we use the following basis set:

$$|\underline{n};l\rangle_v=\frac{1}{2}(v_{n\uparrow}c_{l\uparrow}^{\dagger}+v_{n\downarrow}c_{l\downarrow}^{\dagger})|g\rangle\quad(n,l=1,\ldots,N).\tag{4}$$

Double-core-excited states which may be observed in x-ray pump-probe spectroscopy [18] do not contribute to the CXRS and will not be considered here. To allow spectral

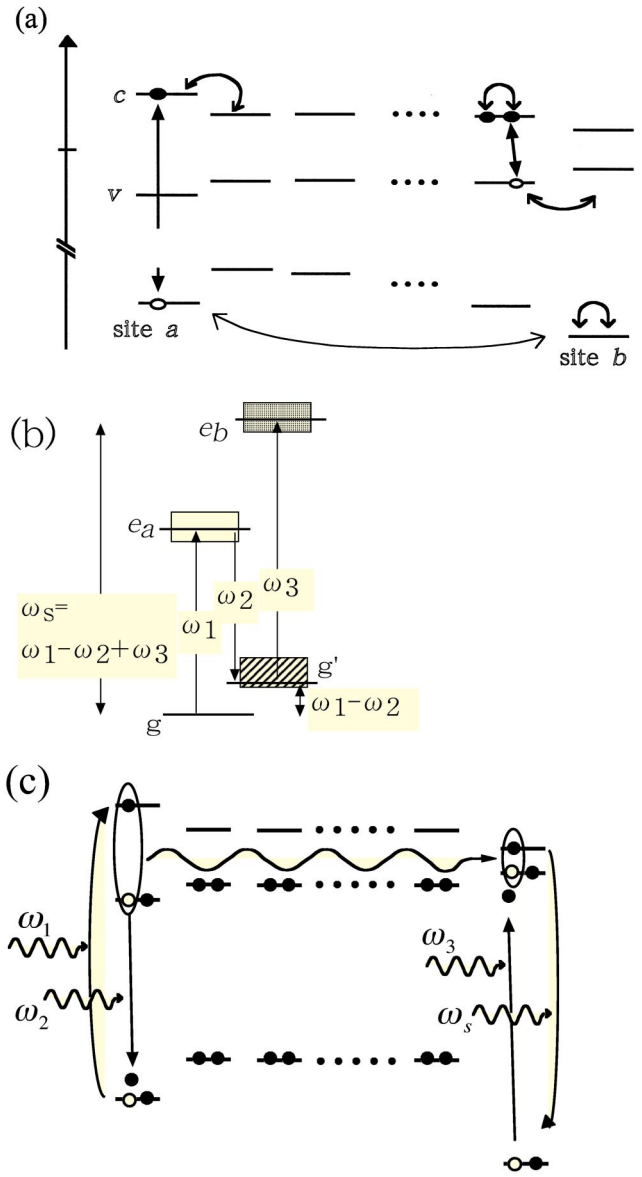

FIG. 1. (a) One-electron picture of the Hamiltonian (equation) and its parameters. (b) The TCXRS described using the many-electron states. (c) The TCXRS process depicted using one-electron energy levels.

selectivity, we assume that the core-excited-state energies of site a (e_a) and site b (e_b) are well separated.

The energy-level scheme for the global (many-electron) states of our model is shown in Fig. 1(b), where e_a and e_b are the core-excited states at site a and b, respectively, and g' denotes the valence-excited states.

The interaction of the molecule with a resonant radiation x-ray field is given by the minimal coupling Hamiltonian [15]

$$\hat{H}_{int}=-\int d\mathbf{r}\hat{j}(\mathbf{r})\cdot\hat{A}(\mathbf{r},t)d\mathbf{r}, \tag{5}$$

where $\hat{A}(\mathbf{r},t)$ is the vector potential and $\hat{j}(\mathbf{r})$ is the atomic current-density operator

$$\hat{j}(\mathbf{r})=\sum_{l=1}^{N}\delta(\mathbf{r}-\mathbf{R}_l)\hat{j}_l. \tag{6}$$

Here, $\mathbf{R}_l$ denotes the lth atomic position, and

$$\hat{j}_l=\sum_{l\sigma}(\mu_l^{ac}a_{l\sigma}c_{l\sigma}^{\dagger}+\mu_l^{av}a_{l\sigma}v_{l\sigma}^{\dagger}+\mu_l^{vc}v_{l\sigma}c_{l\sigma}^{\dagger}+\text{H.c.}), \tag{7}$$

where the atomic current-density operator matrix elements for the ac (core-conduction), av (core-valence), and vc (valence-conduction) transitions at the lth site are denoted by μ_l^{ac}, μ_l^{av}, and μ_l^{vc}, respectively. We only retain the on-site atomic radiative transitions; cross transitions between orbitals at different atomic sites may be safely neglected due to their weak overlap.

Combining Eqs. (1) and (5), the total Hamiltonian is finally given by

$$H_{tot}=H_m+H_{int}. \tag{8}$$

III. THE TIME-RESOLVED COHERENT X-RAY RAMAN SIGNAL

We consider a four-wave-mixing process induced by three x-ray beams. The incoming electric field is

$$\begin{aligned}E(\mathbf{r},t)=&E_1(t+\tau+\tau')\exp[i(\mathbf{k}_1\cdot\mathbf{r}-\omega_1 t)]+E_2(t+\tau)\\&\times\exp[i(\mathbf{k}_2\cdot\mathbf{r}-\omega_2 t)]+E_3(t)\exp[i(\mathbf{k}_3\cdot\mathbf{r}-\omega_3 t)]\\&+E_{LO}(t)\exp[i(\mathbf{k}_{LO}\cdot\mathbf{r}-\omega_{LO}t)]+\text{c.c.}\end{aligned} \tag{9}$$

In the TCXRS process depicted in Fig. 1(c), the valence excitation is created by the $\mathbf{k}_1$ and $\mathbf{k}_2$ pulses, the third $\mathbf{k}_3$ pulse is delayed by τ, and the generated x-ray pulse is heterodyne detected. The TCXRS signal $\omega_s=\omega_1-\omega_2+\omega_3$ is resonant with the core-excited states, and $\omega_1-\omega_2$ is tuned across the optical valence excitation band. The wave vector and the frequency of the local oscillator are taken as $\mathbf{k}_{LO}=\mathbf{k}_s$ and $\omega_{LO}=\omega_s$, respectively. During the delay period the valence excitation created at site a migrates to other atomic sites and the valence exciton is finally detected at site b. The migration of the valence excitation can then be probed through real-time snapshots of the signal.

Our calculations are based on a nonlinear response function formulation of nonlinear x-ray spectroscopy [15] which fully takes into account the spatial and temporal coherence involved in the molecular response to the x-ray radiation fields. We have recently used its frequency domain form, the nonlinear susceptibility $\chi^{(3)}$, to describe the stationary response of the coherent x-ray Raman scatterings [19]. The time-integrated heterodyne TCXRS signal is given by [16]

$$S_{\mathrm{TCXRS}}(\mathbf{k}_s,\tau)=-2\omega_s\mathrm{Im}\int_{-\infty}^{\infty}dtE_{LO}^{*}(t)P^{(3)}(\mathbf{k}_s,t)\times\exp[i(\omega_{\mathrm{LO}}-\omega_s)t], \tag{10}$$

where $P^{(3)}(\mathbf{k}_s,t)$ is the third-order nonlinear polarization described by the nonlinear response function $\mathcal{S}^{(3)}$, given in Appendix A. The seven Liouville space pathways contributing to $\mathcal{S}^{(3)}$ were given in Fig. 13 of Ref. [18].

In all calculations, we assumed that the first two pulses are time coincident, setting $\tau'=0$ and that only the ground state is initiallly populated: $T=0$ (zero temperature). Because of the fast Auger decay, the core-excited state lifetime (<10 fs) is much shorter than the dephasing time and the population decay time of the optically excited states (picosecond to nanosecond). As a result, the dominant contributions to the CXRS come from the R_{IV} pathway [18] which only include the single-core-excited states and the optically excited states; the signal originating from all other pathways is rapidly attenuated because of the fast Auger decay process. Retaining the R_{IV} contribution in Eqs. (A10), we obtain

$$\begin{aligned}S_{\mathrm{TCXRS}}(\mathbf{k}_s;\tau)&\simeq S_{IV}(\mathbf{k}_s;\tau)\\&=\frac{-2}{\hbar^3}\frac{1}{\omega_3\omega_2\omega_1\omega_s}\mathrm{Im}\int_{-\infty}^{\infty}dt\int_0^{\infty}dt_3\int_0^{\infty}dt_2\\&\times\int_0^{\infty}dt_1R_{IV}(-\mathbf{k}_s;\mathbf{k}_3,-\mathbf{k}_2,\mathbf{k}_1,t_3,t_2,t_1)\\&\times\exp[i(\omega_3-\omega_2+\omega_1)t_3-i(\omega_2-\omega_1)t_2\\&+i\omega_1t_1]E_{LO}^{*}(t)E_3(t-t_3)E_2^{*}(t+\tau-t_3-t_2)\\&\times E_1(t+\tau-t_3-t_2-t_1),\end{aligned} \tag{11}$$

where

$$R_{IV}=\langle\hat{j}(\mathbf{r},t_1+t_2+t_3)\hat{j}(\mathbf{r}_3,t_1+t_2)\hat{j}(\mathbf{r}_2,t_1)\hat{j}(\mathbf{r}_1,0)\rangle. \tag{12}$$

A closed expression for the signal in terms of the multipoint (time and space) correlation functions is given in Appendix A.

Expanding Eq. (12) in the eigenstates of H_m, and assuming that the first pair of pulses, $\mathbf{k}_1$ and $\mathbf{k}_2$, is well separated from the other pair, $\mathbf{k}_3$ and $\mathbf{k}_s$, leads to a doorway-window expression for the TCXRS [16,35],

$$S_{\mathrm{TCXRS}}(\mathbf{k}_s;\tau)=\frac{2}{\hbar}\mathrm{Re}\sum_{g'}W_{gg'}(\omega_1,\omega_2,\omega_3)\times\exp[i(\omega_1-\omega_2)\tau]I_{g'g}(\tau)D_{g'g}(\omega_1,\omega_2). \tag{13}$$

Here, $D_{g'g}(\omega_1,\omega_2)$ is the *doorway function* representing the exciton wave packet created by the first pair of pulses

$$D_{g'g}(\omega_1,\omega_2)\equiv\frac{i}{\hbar}\sum_{e=e_a,e_b}J_{ge;eg'}^{*}(\mathbf{k}_1-\mathbf{k}_2)\int_{-\infty}^{\infty}dt'\int_0^{\infty}dt_1\times\exp[i(\omega_2-\omega_1)t'+i\omega_1t_1]E_2^{*}(t')\times E_1(t'-t_1)I_{g'g}(-t')I_{eg}(t_1) \tag{14}$$

and $W_{gg'}(\omega_1,\omega_2,\omega_3)$ is the *window function* representing the generation of the signal,

$$\begin{aligned}W_{gg'}(\omega_1,\omega_2,\omega_3)\equiv\frac{i}{\hbar}\sum_{e=e_a,e_b}J_{ge;eg'}(\mathbf{k}_1-\mathbf{k}_2)\int_{-\infty}^{\infty}dt\int_0^{\infty}dt_3&\times\exp[-i(\omega_2-\omega_1)t+i(\omega_3-\omega_2\\&+\omega_1)t_3]\\&\times E_{LO}^{*}(t+t_3)E_3(t)I_{eg}(t_3)I_{g'g}(t),\end{aligned} \tag{15}$$

where $J_{ab;cd}(\mathbf{k})$ is a tetradic current-density matrix defined as [18,20]

$$J_{ab;cd}(\mathbf{k})\equiv\int d\mathbf{r}j_{ab}(\mathbf{r})j_{cd}^{*}(\mathbf{r})\exp(-i\mathbf{k}\cdot\mathbf{r}). \tag{16}$$

The doorway-window expression connects the signal with the exciton wave packet motion and offers the following physical picture for the TCXRS process: The state of the system in the valence-exciton manifold is described by the density operator. It evolves during t_1, creating a doorway wave packet which then evolves for the delay period τ. During t_3, a *window wave packet* is formed and the TCXRS response is finally given by the Liouville space overlap of the doorway wave packet with the window wave packet.

In our simulations, we have included the finite pulse durations by assuming rectangular x-ray pulses with duration δ_1 for $\mathbf{k}_1$ and $\mathbf{k}_2$, and δ_2 for $\mathbf{k}_3$ and $\mathbf{k}_s$. Equations (14) and (15) then assume the form

$$\begin{aligned}D_{g'g}(\omega_1,\omega_2)=\frac{i}{\hbar}\sum_{e=e_a,e_b}J_{ge;eg'}^{*}(\mathbf{k}_1-\mathbf{k}_2)\frac{2}{i(\omega_{eg}-\omega_1)+\Gamma}&\times\left\{\frac{\sinh\{[i(\omega_{g'g}-\omega_1+\omega_2)+\gamma]\delta_1/2\}}{i(\omega_{g'g}-\omega_1+\omega_2)+\gamma}\right.\\&-\frac{\sinh\{[i(\omega_{eg'}-\omega_2)+(\Gamma-\gamma)]\delta_1/2\}}{i(\omega_{eg'}-\omega_2)+(\Gamma-\gamma)}\\&\left.\times\exp\{-i[(\omega_{eg}-\omega_1)+\Gamma]\delta_1/2\}\right\},\end{aligned} \tag{17}$$

and

$$W_{gg'}(\omega_1,\omega_2,\omega_3) = \frac{i}{\hbar}\sum_{e=e_a,e_b} J_{ge;eg'}(\mathbf{k}_1-\mathbf{k}_2) \times \frac{2}{i(\omega_{eg'}-\omega_3)+(\Gamma-\gamma)} \times \left\{ \frac{\sinh\{[i(\omega_{g'g}-\omega_1+\omega_2)+\gamma]\delta_2/2\}}{i(\omega_{g'g}-\omega_1+\omega_2)+\gamma} - \frac{\sinh\{[i(\omega_{eg}-\omega_s)+\Gamma]\delta_2/2\}}{i(\omega_{eg}-\omega_s)+\Gamma} \times \exp\{-i[(\omega_{eg'}-\omega_3)+(\Gamma-\gamma)]\delta_2/2\} \right\}. \quad (18)$$

It is interesting to note that the TCXRS signal only depends on the scattering wave vector $\mathbf{q}\equiv\mathbf{k}_1-\mathbf{k}_2$, unlike the coherent optical Raman scattering, where the signal field generated at $\mathbf{k}_s=\mathbf{k}_3-\mathbf{k}_2+\mathbf{k}_1$ depends on $\mathbf{k}_3$ as well. This can be rationalized as follows: In Eq. (A6d) for the R_{IV} Liouville pathways, we must set $\mathbf{r}=\mathbf{r}_3$ because the core-to-valence transitions $j_{ab}(\mathbf{r})$ and $j_{bc}(\mathbf{r}_3)$ should take place at the same atomic site, leading to $\mathbf{r}=\mathbf{r}_3$. Similarly, we set $\mathbf{r}_2=\mathbf{r}_1$. As a result, the $\mathbf{k}_3$ dependence drops out. The $\mathbf{q}$ dependence, comes through the factor $\exp[\mathbf{q}\cdot(\mathbf{r}-\mathbf{r}_1)]$, where $\mathbf{r}_1$ and $\mathbf{r}$ denote the positions where the doorway wave packet and the window wave packet are created, respectively.

IV. NUMERICAL SIMULATIONS

The valence and conduction orbital energies are chosen such that the Frenkel exciton frequency, determined by the energy difference between the conduction and valence orbitals at each atomic site, is the highest at site *a* and the lowest at site *b*, creating an energy gradient from site *a* toward site *b*, as is often seen in a donor acceptor push-pull polyenes [29]. The core orbital energy is specific to each element and we took the core orbital energy of site *a* to be 100 eV lower than of site *b*: this mimics for example, nitrogen and oxygen 1*s* core orbital energies which are about 400 eV and 500 eV, respectively.

A. X-ray- and optical-absorption spectra

Figure 2(a) shows the x-ray-absorption spectra corresponding to the transition of core electrons to the unoccupied conduction levels. The absorption lines of site *a* and *b* are around 100 eV and 200 eV, respectively. The lowest intense (104.6 eV and 203.8 eV) peaks correspond to core excitons, in which the excited electrons from the core orbitals are strongly localized at the same site due to the large core-exciton coupling.

Figure 2(b) depicts the calculated optical-absorption spectrum. Since, we assume a rather strong 7 eV Coulomb interaction between a valence hole and a conduction electron, the Frenkel exciton states where the conduction electron and valence hole strongly bind at an atomic site lie below the scattering state, where both particles reside at different atomic sites. The Frenkel exciton absorption lines are, therefore, below 10 eV, as shown in Fig. 2(c) on an expanded scale. The intensity is sharply peaked at the lowest Frenkel exciton, and the other peaks are rather weak, which is characteristic of one-dimensional molecular chains [29]. If all atoms were equivalent, because of inversion symmetry, only lines with solid bars would be optically allowed. Here, since we have different atoms at both ends, this selection rule is broken and absorption lines due to the Raman active mode marked by dashed bars have finite but weak intensities. The frequency-domain CXRS technique clearly resolves the Frenkel exciton and the scattering states which are not well separated in the optical-absorption spectrum [19].

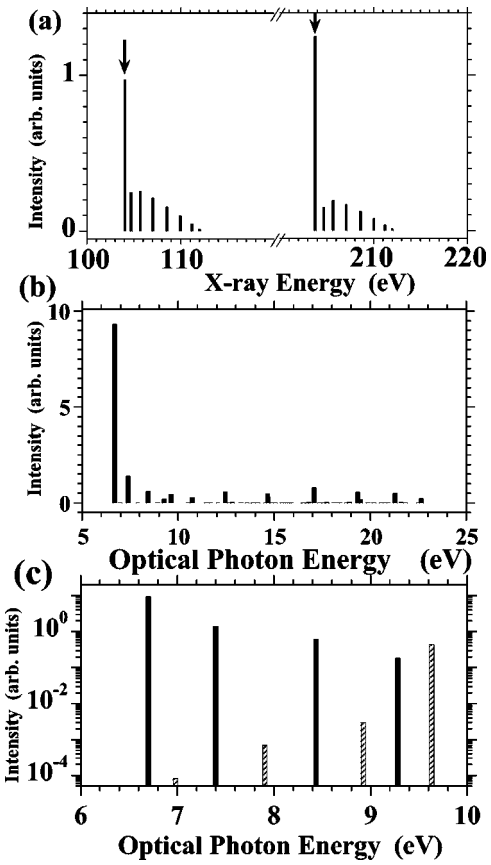

FIG. 2. (a) The x-ray-absorption spectrum. (b) The optical-absorption spectrum. (c) The optical-absorption spectrum for the Frenkel exciton states depicted on a log scale using an expanded frequent scale.

B. Time-resolved CXRS

In Fig. 3(a), we display the variation of the time-resolved CXRS spectra with the time delay τ, where ω_1 is fixed at the *a* core exciton peak and ω_s is tuned to the *b* core exciton. We have neglected charge redistribution effects, known as shake-up processes [36,37] induced by core excitation. The reason is that in the present model, the core electron is resonantly excited to a strongly bound core-exciton state, where charge neutrality around the excited atom is maintained. Va-

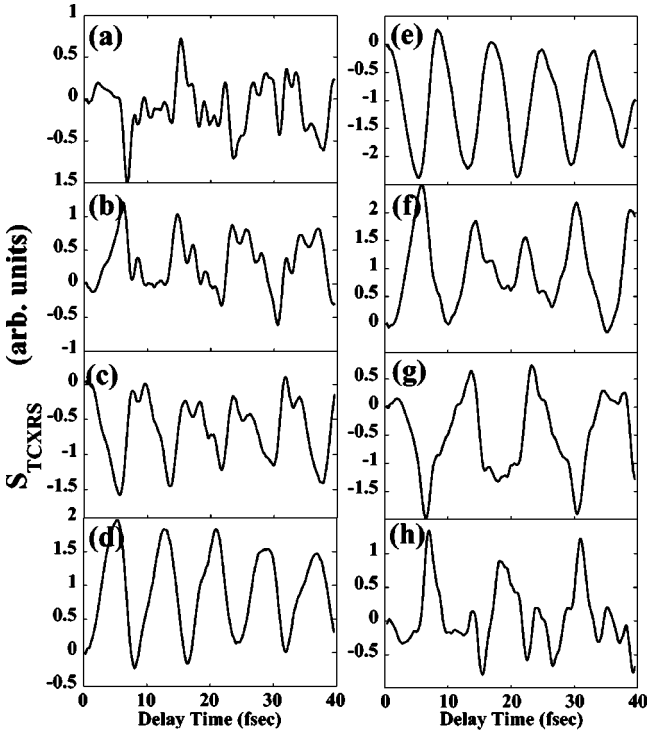

FIG. 3. TCXRS versus time delay τ for all eight Frenkel exciton states arranged by energy from (a) to (h) when ω_1 and ω_s are tuned at the *a* core-exciton peak and *b* core-exciton peak, respectively.

lence relaxation becomes important only when the core electron is excited to the high-energy continuum, the molecule is ionized, and the Coulomb potential of the core hole potential strongly affects the electronic levels by creating shake-up states. The pulse durations are $\delta_1=5$ fs for $\mathbf{k}_1$ and $\mathbf{k}_2$, and $\delta_2=0.5$ fs for $\mathbf{k}_3$ and $\mathbf{k}_s$. In all the calculations, we took $\Gamma=64$ meV corresponding to C 1*s* core hole lifetime due to Auger decay ($\sim$10 fs) and $\gamma=1$ meV, corresponding to a typical electronic dephasing time for conjugated molecules ($\sim$0.7 ps).

Since the highly localized core hole does not migrate [34], the valence exciton is created at site *a* by the combined action of the $\mathbf{k}_1$ and $\mathbf{k}_2$ beams, and annihilated at site *b* by $\mathbf{k}_3$ and $\mathbf{k}_s$, as shown in Fig. 1. The TCXRS signal then becomes large when the valence hole and the conduction electron are located at the same site, i.e., site *a* or *b* forming a Frenkel exciton. In Fig. 3, we tune $\omega_1-\omega_2$ to (a) 6.70 eV, (b) 6.98 eV, (c) 7.40 eV, (d) 7.90 eV, (e) 8.44 eV, (f) 8.92 eV, (g) 9.28 eV, and (h) 9.63 eV, corresponding to the eight Frenkel exciton peaks in Fig. 2(c), respectively. The temporal profile of the TCXRS signal strongly depends on $\omega_1-\omega_2$, reflecting the real-time wave-packet motion for each valence exciton. The periodic change of the signal clearly seen in Figs. 3(b) to 3(f) corresponds to the back-and-forth valence-exciton motion.

In Fig. 4(a) and 4(b), we display the Fourier transforms of the signals shown in Figs. 3(a) and 3(e), where $\omega_1-\omega_2$ is held fixed at the first (6.70 eV) and fifth (8.44 eV) Frenkel exciton states, respectively. We observe quantum beats between different valence-excitons excited coherently by the x-ray pulses $\mathbf{k}_1$ and $\mathbf{k}_2$. When $\omega_1-\omega_2$ is tuned to a particular

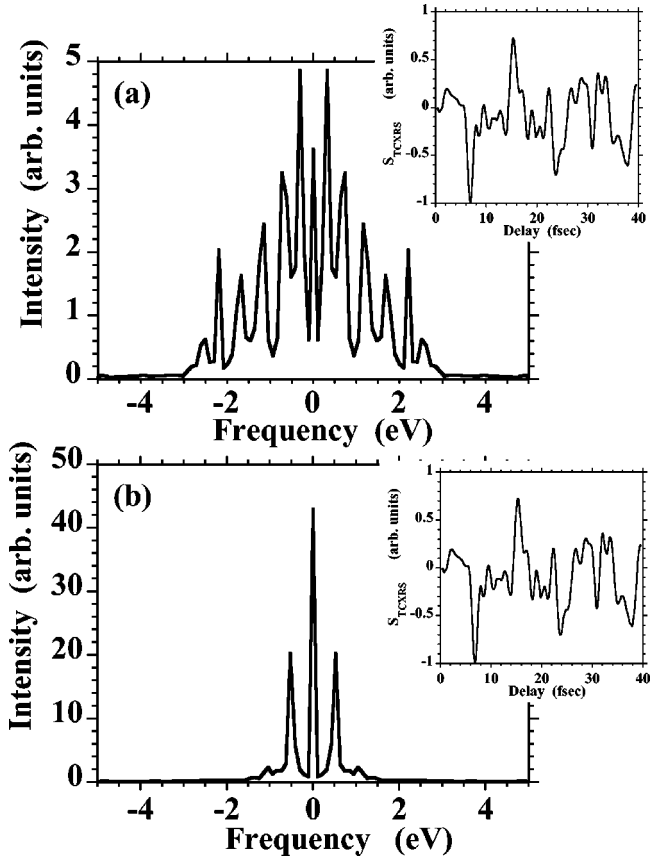

FIG. 4. The Fourier transform of the TCXRS when $\omega_1-\omega_2=6.7$ eV (a) and 8.44 eV (b), corresponding to the first and the fifth Frenkel exciton states, respectively. The corresponding time resolved spectra are shown in the insets.

exciton-state energy $\omega_{\underline{g}}$, Eq. (13) may be recast in the form

$$S_{\mathrm{TCXRS}}(\mathbf{k}_s;\tau:\omega_1-\omega_2=\omega_{\underline{g}}) = \frac{2}{\hbar}\mathrm{Re}\sum_{g'} W_{gg'}(\omega_1,\omega_2,\omega_3) \times \exp[-i(\omega_{g'}-\omega_{\underline{g}})\tau-\gamma\tau]D_{g'g}(\omega_1,\omega_2). \quad (19)$$

The time evolution of the TCXRS is caused by quantum beats between the valence-excitons around the tuned exciton by $\omega_1-\omega_2=\omega_{\underline{g}}$. The doorway function $D_{g'g}(\omega_1,\omega_2)$ in Eq. (19) determines the probability of the coherent excitation of the valence-excitons which depends upon the pulse frequencies, ω_1 and ω_2, and durations, δ_1.

To illustrate the connection between the TCXRS and the exciton wave packet motion in Liouville space, we have computed the time evolution of the exciton density operator

$$\rho_{IV}(\omega_1,\omega_2;\tau) = \exp[i(\omega_1-\omega_2)\tau]\sum_{g'} I_{g'g}(\tau)D_{g'g}(\omega_1,\omega_2)|g'\rangle\langle g|. \quad (20)$$

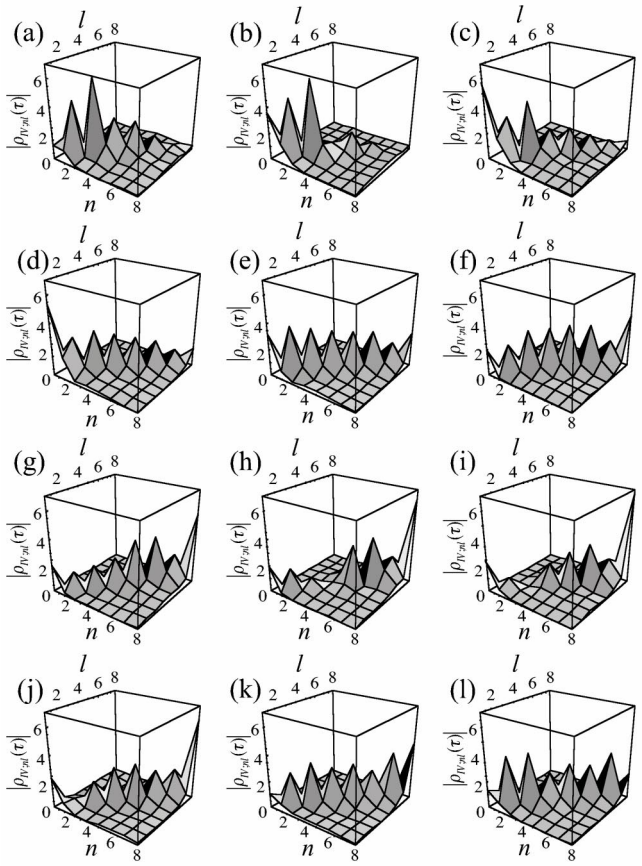

FIG. 5. Time evolution of the density operator for $\omega_1-\omega_2=8.44$ eV. Shown is $|\rho_{IV;nl}(\tau)|$ in a common arbitrary unit. The time delay τ is varied from 0 fs to 6.6 fs in (a)–(l). n and l axes are labeled by the atomic site number for the valence hole and conduction electron, respectively.

The reduced density operator is given by

$$\rho_{IV;nl}(\tau)=\sum_{\sigma}\ \mathrm{Tr}[c_{n\sigma}v^{\dagger}_{l\sigma}\rho_{IV}(\omega_1,\omega_2;\tau)], \qquad (21)$$

where the diagonal and the off-diagonal matrix elements represent the induced charge density and the dynamical bond order corresponding to the valence-exciton wave packet [30,38].

Figures 5(a–l), depicts the time evolution of $\rho_{IV;nl}(\tau)$ when $\omega_1-\omega_2=8.44$ eV is tuned to the fifth Frenkel exciton state. Since the first two x-ray beams create a Frenkel exciton, the Frenkel exciton component represented by the diagonal element is larger than the scattering state component (off-diagonal element) in which the valence hole and the conduction electron are separated. If $\omega_1-\omega_2$ is tuned to the scattering exciton state, the off-diagonal elements are expected to be dominant. As we proceed from (a) to (f), the population of the valence-exciton spreads over the entire molecule [(e) and (f)]; it is localized on site b in (h) and (i), and then the wave packet spreads again over the entire molecule [(k) and (l)]. This coherent exciton motion lasts until the electronic coherence of the valence-exciton decays due to dephasing, as determined by the inverse linewidth $\gamma=1$ meV.

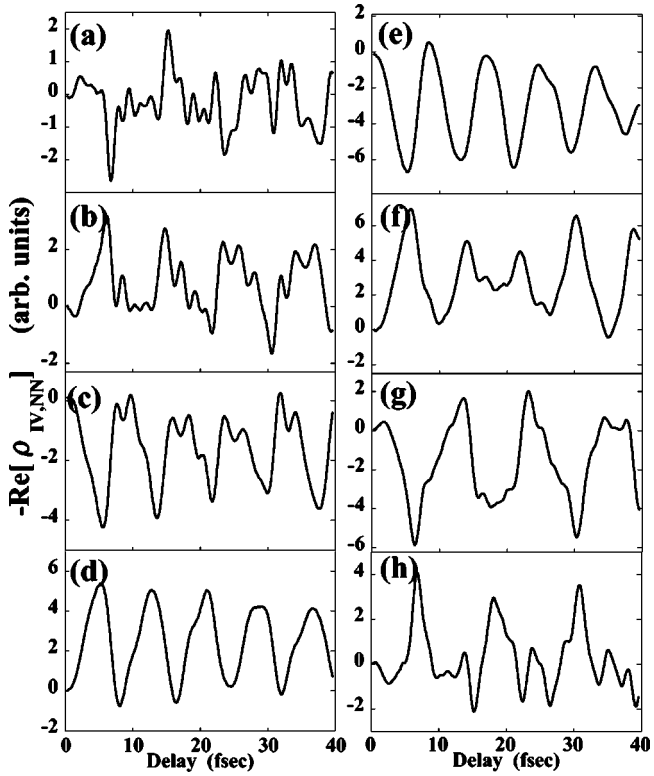

FIG. 6. Time evolution of the diagonal element of the density operator $-\mathrm{Re}[\rho_{IV;NN}(\tau)]$ for the same $\omega_1-\omega_2$ values as in Fig. 3.

Since the third x-ray beam is resonant with the b core exciton, the time evolution of the TCXRS directly probes this valence-exciton wave packet at site b, as shown in Appendix C. In Fig. 6, we present the time evolution of $\rho_{IV;NN}(\tau)$ when $\omega_1-\omega_2$ are held fixed at the same Frenkel exciton states as in Fig. 3. The close correlation between Fig. 3 and Fig. 6 clearly demonstrates that the TCXRS is an excellent *local* probe of the valence-exciton wave-packet motion. By tuning ω_s to the a core exciton, we can observe the exciton wave-packet motion at site a where the window wave packet is created.

In Fig. 7, we display the time-resolved CXRS spectra as a function of the delay τ, where ω_1 and ω_s are tuned to the core-exciton peak of site a. Values of $\omega_1-\omega_2$ at (a) 6.70 eV, (b) 6.98 eV, (c) 7.40 eV, (d) 7.90 eV, (e) 8.44 eV, (f) 8.92 eV, (g) 9.28 eV, and (h) 9.63 eV, correspond to the eight Frenkel exciton peaks in Fig. 2(c), respectively. The temporal profiles of Fig. 7 are quite different from Fig. 3. The TCXRS signal of Fig. 7 correlates well with the density matrix elements $\rho_{IV:11}$ (not shown). This clearly demonstrates that the TCXRS is a local sensitive probe that can detect the exciton wave-packet motion at any selected atomic site by simply tuning the detected x-ray energies to the core-exciton peak at that site.

To illustrate the effect of the probe duration δ_2, we show in Fig. 8 the TCXRS for $\delta_2=5$ fs: Figs. 8 (a) and 8(b) correspond to the case of Fig. 3(b) and Fig. 7(b), respectively,

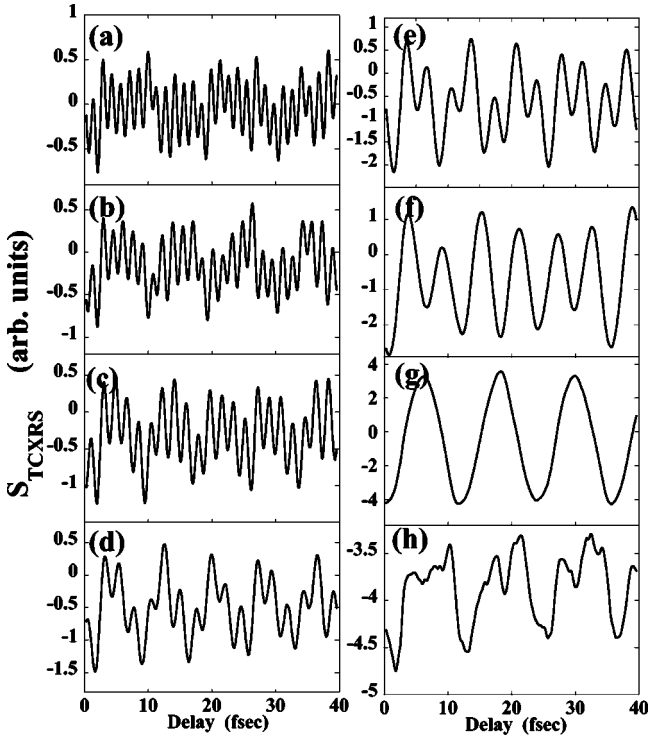

FIG. 7. TCXRS versus time delay τ for all eight-Frenkel-exciton states in (a)–(h), when ω_1 and ω_s are both tuned at the *a* core-exciton peak.

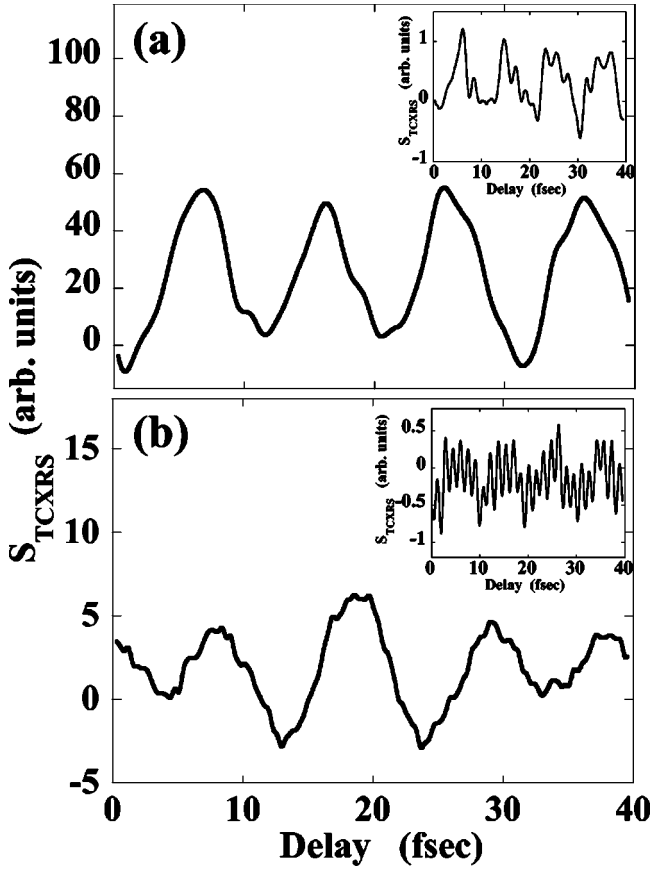

FIG. 8. TCXRS for $\omega_1-\omega_2=6.98$ eV (the fourth Frenkel exciton): (a) ω_1 and ω_s are fixed at the core-exciton peaks of *a* and *b* sites, respectively, (b) ω_1 and ω_s are both fixed core-exciton state at the *a* site. The pulse duration δ_2 is 5 fs.

where $\delta_2=0.5$ fs are used. The $\delta_2=0.5$ fs signals are also shown in the inset for comparison. Since the TCXRS is obtained by the overlap of the doorway wave packets propagated during τ with the window function, the rapid change in the wave packet is averaged out in Fig. 8, but the low-frequency oscillation can still be seen.

Finally, we examine the **q** dependence of the TCXRS. This dependence comes through the $\exp[\mathbf{q}\cdot(\mathbf{r}-\mathbf{r}_1)]$ factor, where $\mathbf{r}_1$ and $\mathbf{r}$ denote the positions where the doorway wave packet and the window wave packets are created, respectively. Since we only considered fields resonant with two core orbitals at both end atoms, the TCXRS shows **q** dependence only when the first two x-ray beams, ($\mathbf{k}_1$ and $\mathbf{k}_2$), are resonant with the core-excited state of site *a*, while the other two are resonant with the core-excited states of site *b*, as is the case in Fig. 3. The wave-vector dependence of the TCXRS for Fig. 3(d) is shown in Fig. 9, $\mathbf{q}=2\pi/L\cdot j$ is taken as (a) $j=0$, (b) $j=0.1$, (c) $j=0.2$, (d) $j=0.3$, (e) $j=0.4$, (f) $j=0.5$. Varying **q** is equivalent to changing the phase relation between the x-ray pulses, making it possible to investigate the amplitude as well as the phase of the induced third-order nonlinear polarization.

For molecules with several sites with nearly degenerate core-exciton energies the **q** dependence is not merely through the phase and the **q** dependence of the signal through Eqs. (13), (14), and (15) should carry a direct signature of excitation transport. Optical transient grating experiments of excitations are commonly used to observe long-wavelength diffusion [16,39]. Attempts to use this technique to probe coherent exciton motion in molecular crystals at low temperatures were not successful [39], since the long-wavelength dynamics was dominated by polaritons [40,41]. X-ray gratings such as in the CXRS should allow to probe the dynamics of excitations on much finer length scales, making it possible to observe coherent exciton motions.

V. CONCLUDING REMARKS

In this paper, we have formulated the time-resolved CXRS in terms of nonlinear response functions involving the electronic current. Numerical simulations demonstrate how the real-time dynamics of the valence-exciton wave packet in a one-dimensional molecular chain may be investigated with an atomic scale precision: By tuning the x-ray frequencies across a core resonance, we can probe the time evolution of the valence-exciton wave packet at selected atomic sites. The technique thus provides real-time snapshots of valence-exciton motion. This is in contrast with SXRS which takes place at a single atomic site because the core hole is localized and is immobile. Consequently, SXRS cannot observe the spatial coherence among separated atomic sites [20].

Optical four-wave-mixing spectroscopy has been widely used to investigate exciton transport in semiconductors and molecules [29,42]. Recent experiments revealed the important role of many-body correlations of excitons which cannot

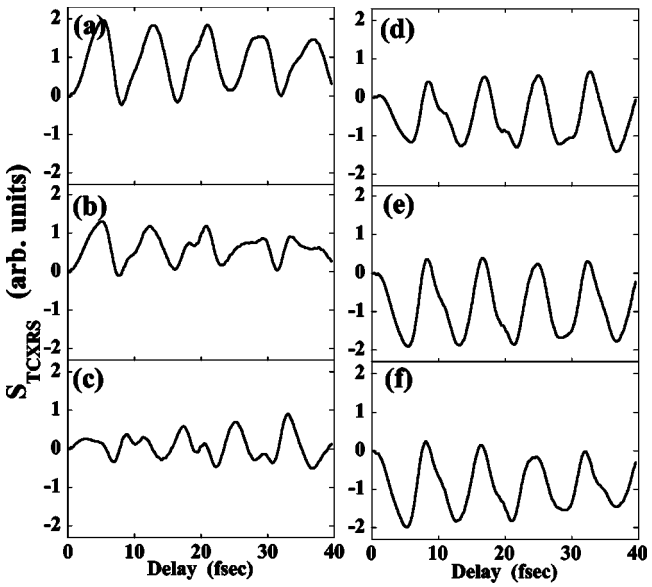

FIG. 9. The wave vector **q** dependence of the TCXRS for the signals shown in Fig. 3(d). The scattering wave vector $\mathbf{q}=2\pi/L\cdot j$ is (a) $j=0$, (b) $j=0.1$, (c) $j=0.2$, (d) $j=0.3$, (e) $j=0.4$, (f) $j=0.5$.

be explained by a simple model of noninteracting two-level systems within the local-field approximation [43,44]. In many conjugated molecules, exciton-exciton interactions as well as exciton-phonon couplings play an important role in the relaxation dynamics [29,39,42–45]. Probing the spatial and temporal coherence of excitons would be a most valuable tool in the investigation of these mesoscopic materials. While in optical nonlinear spectroscopy the spatial information on exciton transport is highly averaged due to the long-wavelength limit, the TCXRS observes the temporal evolution of spatial coherence of valence-excitons between different atomic sites with atomic resolution. This is illustrated by our simulations.

The important molecular time scales of our system are the dephasing time $\tau_d(\leqslant 1$ ps), the population decay times of the valence-exciton states $\tau_p(\sim 10$ ps) and the core excited states $\tau_c(\leqslant 10$ fs); Usually $\tau_c \ll \tau_d \ll \tau_p$. Very recently Drescher *et al.* have generated x-ray pulse with the 0.5 fs duration by high harmonic generation, and observed time-resolved Auger emission spectrum with the time resolution of 7 fs [46]. Such x-ray pulses are shorter than τ_d, making it possible to investigate the valence-exciton transport in real time.

In order to observe the nonlinear response in the x-ray regime, the field intensity should be sufficiently high. In Ref. [19], we gave a crude estimate for the magnitude of the resonant $\chi^{(3)}$. Using the C $1s\rightarrow 2p$ atomic dipole transitions in polydiacetylene (PDA), we found it to be about 3.5×10^{-12} esu under fully resonant conditions, where we have used 6.2×10^{-29} esu for the atomic dipole transition, 0.032 eV for C $1s$ Auger decay lifetime broadening, 0.03 eV for the lifetime broadening of the optical excited state (^1B_u state in PDA), and 1.7×10^{-21} cm^{-3} for the density of molecule. This is 2 to 3 orders of magnitude smaller than $\chi^{(3)}$ in the optical region [47]. However, recent progress in the generation of intense femtosecond spatially coherent x-ray pulses by high harmonic generation should make these measurements possible [48].

Since the present calculation was carried out using the sum-over states expression for NRF, electron correlation effects may be fully taken into account. We restricted the calculation to small molecules in order to illustrate the potential of the TCXRS. As the molecular size increases, however, computing the exact global eigenstates of the system becomes a formidable task. Since what we can actually observe are multitime correlation functions, the complete information about the exact eigenstates is redundant. Instead, we can adopt a different strategy based on solving the equations of motion for the appropriate many-particle Green functions to obtain the reduced density matrix [16]. The collective electron oscillator method based on the time-dependent density functional or the time-dependent Hartree-Fock has proven very useful for nonlinear optical spectroscopy [30,38]. Extending these techniques to the x-ray regime by incorporating the core levels should allow to extend the present calculations to more complex systems.

An interesting future extension of this work would be to include time resolved shake-up effects. In x-ray absorption, the x-ray excited electron will partially screen the core hole, such that the shake-up response of the many electron system is strongly dependent on the energy of the excited electron; and in fact, near threshold the screening is largely complete and little shake-up occurs. With time resolved x-ray spectroscopies, it should be possible to observe the decrease in this screening as the excited electron leaves, and the subsequent onset of shake-up excitations. Similar screening effects occur in photoemission and the time resolution of photoemission shake-up could likewise be observed [49–52].

ACKNOWLEDGMENTS

The support of the Chemical Science Division of the Office of Basic Energy Science of the U.S. Department of Energy, Grant No. DE-FG02-01ER15155, is gratefully acknowledged. This work was partly supported by a Grant-in-Aid for Scientific Research from the Ministry of Education, Science, Sports, and Culture in Japan.

APPENDIX A: NONLINEAR RESPONSE FUNCTIONS FOR TCXRS

Below we give explicit expressions of the correlation functions for the third-order nonlinear polarization. In the heterodyne detection of the time-resolved four-wave mixing, the external electrical field may be represented as

$$E(\mathbf{r},t)=E_1(t+\tau+\tau')\exp(i\mathbf{k}_1\cdot\mathbf{r}-i\omega_1 t)+E_2(t+\tau)\times\exp(i\mathbf{k}_2\cdot\mathbf{r}-i\omega_2 t-i\phi)+E_3(t)\exp(i\mathbf{k}_3\cdot\mathbf{r}-i\omega_3 t)+E_{\mathrm{LO}}(t)\exp(i\mathbf{k}_{LO}\cdot\mathbf{r}-i\omega_{LO}t-i\psi)+\mathrm{c.c.}, \quad \text{(A1)}$$

where we have assumed a phase control of the pulses. In Eq. (A1), ϕ is the relative phase of E_2 with respect to E_1, and ψ

is the phase of the local oscillator with respect to E_3. In the present applications, we assume $\phi=\psi=0$ and $\tau'=0$.

The third-order nonlinear polarization $P^{(3)}(\mathbf{r},t)$ is given by Eq. (A2) in Ref. [18]. Fourier transform with respect to $\mathbf{r}$ gives

$$\begin{aligned}P^{(3)}(\mathbf{k}_s,t)&\equiv\int d\mathbf{r}P^{(3)}(\mathbf{r},t)\exp[-i\mathbf{k}_s\cdot\mathbf{r}]\\&=\int dt_3\int dt_2\int dt_1\mathcal{S}^{(3)}(-\mathbf{k}_s;\mathbf{k}_3,\mathbf{k}_2,\mathbf{k}_1,t_3,t_2,t_1)\\&\quad\times E(t-t_3)E(t-t_3-t_2)E(t-t_3-t_2-t_1),\end{aligned}\tag{A2}$$

where $\omega_s\equiv\omega_1+\omega_2+\omega_3$ and $\mathbf{k}_s\equiv\mathbf{k}_1+\mathbf{k}_2+\mathbf{k}_3$. In Eq. (A2), $\mathcal{S}^{(3)}(-\mathbf{k}_s;\mathbf{k}_3,\mathbf{k}_2,\mathbf{k}_1,t_3,t_2,t_1)$ is defined as the multidimensional Fourier transform of $\mathcal{S}^{(3)}(\mathbf{r};\mathbf{r}_3\mathbf{r}_2\mathbf{r}_1t_3t_2t_1)$

$$\begin{aligned}\mathcal{S}^{(3)}(-\mathbf{k}_s;\mathbf{k}_3,\mathbf{k}_2,\mathbf{k}_1,t_3,t_2,t_1)&\equiv\int d\mathbf{r}\int d\mathbf{r}_3\int d\mathbf{r}_2\int d\mathbf{r}_1\mathcal{S}^{(3)}(\mathbf{r};\mathbf{r}_3\mathbf{r}_2\mathbf{r}_1t_3t_2t_1)\\&\quad\times\exp[-i\mathbf{k}_s\cdot\mathbf{r}+i\mathbf{k}_3\cdot\mathbf{r}_3+i\mathbf{k}_2\cdot\mathbf{r}_2+i\mathbf{k}_1\cdot\mathbf{r}_1].\end{aligned}\tag{A3}$$

Substituting the form of $\mathcal{S}^{(3)}(\mathbf{r};\mathbf{r}_3\mathbf{r}_2\mathbf{r}_1t_3t_2t_1)$ given by Eq. (A6) in Ref. [18] into Eq. (A3), we then have

$$\begin{aligned}&\mathcal{S}^{(3)}(-\mathbf{k}_s;\mathbf{k}_3,\mathbf{k}_2,\mathbf{k}_1,t_3,t_2,t_1)\\&=\frac{1}{\hbar^3(\omega_1\omega_2\omega_3\omega_s)}\sum_{\alpha=1}^{4}[R_\alpha(-\mathbf{k}_s;\mathbf{k}_3,\mathbf{k}_2,\mathbf{k}_1,t_3,t_2,t_1)\\&\quad+R_\alpha^*(\mathbf{k}_s;-\mathbf{k}_3,-\mathbf{k}_2,-\mathbf{k}_1,t_3,t_2,t_1)],\end{aligned}\tag{A4}$$

where the response function in the frequency domain is defined similar to Eq. (A3) by

$$\begin{aligned}&R_\alpha(-\mathbf{k}_s;\mathbf{k}_3,\mathbf{k}_2,\mathbf{k}_1,t_3,t_2,t_1)\\&\equiv(-i)^3\int d\mathbf{r}\int d\mathbf{r}_3\int d\mathbf{r}_2\int d\mathbf{r}_1R_\alpha(\mathbf{r};\mathbf{r}_3\mathbf{r}_2\mathbf{r}_1t_3t_2t_1)\\&\quad\times\exp[-i\mathbf{k}_3\cdot(\mathbf{r}-\mathbf{r}_3)-i\mathbf{k}_2\cdot(\mathbf{r}-\mathbf{r}_2)-i\mathbf{k}_1\cdot(\mathbf{r}-\mathbf{r}_1)].\end{aligned}\tag{A5}$$

Using the expression of the response functions given in Eqs. (A7) in Ref. [18], we have

$$\begin{aligned}R_1(-\mathbf{k}_s;\mathbf{k}_3,\mathbf{k}_2,\mathbf{k}_1,t_3,t_2,t_1)&=i\sum_{abcd}P(a)\int d\mathbf{r}\int d\mathbf{r}_3\int d\mathbf{r}_2\int d\mathbf{r}_1j_{cd}(\mathbf{r})j_{da}(\mathbf{r}_1)\\&\quad\times j_{ab}(\mathbf{r}_2)j_{bc}(\mathbf{r}_3)\exp[-i\mathbf{k}_3\cdot(\mathbf{r}-\mathbf{r}_3)-i\mathbf{k}_2\cdot(\mathbf{r}-\mathbf{r}_2)-i\mathbf{k}_1\cdot(\mathbf{r}-\mathbf{r}_1)]I_{dc}(t_3)I_{db}(t_2)I_{da}(t_1),\end{aligned}\tag{A6a}$$

$$\begin{aligned}R_2(-\mathbf{k}_s;\mathbf{k}_3,\mathbf{k}_2,\mathbf{k}_1,t_3,t_2,t_1)&=i\sum_{abcd}P(a)\int d\mathbf{r}\int d\mathbf{r}_3\int d\mathbf{r}_2\int d\mathbf{r}_1j_{cd}(\mathbf{r})j_{da}(\mathbf{r}_1)j_{ab}(\mathbf{r}_2)j_{bc}(\mathbf{r}_3)\\&\quad\times\exp[-i\mathbf{k}_3\cdot(\mathbf{r}-\mathbf{r}_3)-i\mathbf{k}_2\cdot(\mathbf{r}-\mathbf{r}_2)-i\mathbf{k}_1\cdot(\mathbf{r}-\mathbf{r}_1)]I_{dc}(t_3)I_{db}(t_2)I_{ab}(t_1),\end{aligned}\tag{A6b}$$

$$\begin{aligned}R_3(-\mathbf{k}_s;\mathbf{k}_3,\mathbf{k}_2,\mathbf{k}_1,t_3,t_2,t_1)&=i\sum_{abcd}P(a)\int d\mathbf{r}\int d\mathbf{r}_3\int d\mathbf{r}_2\int d\mathbf{r}_1j_{cd}(\mathbf{r})j_{da}(\mathbf{r}_3)j_{ab}(\mathbf{r}_1)j_{bc}(\mathbf{r}_2)\\&\quad\times\exp[-i\mathbf{k}_3\cdot(\mathbf{r}-\mathbf{r}_3)-i\mathbf{k}_2\cdot(\mathbf{r}-\mathbf{r}_2)-i\mathbf{k}_1\cdot(\mathbf{r}-\mathbf{r}_1)]I_{dc}(t_3)I_{ac}(t_2)I_{ab}(t_1),\end{aligned}\tag{A6c}$$

$$\begin{aligned}R_4(-\mathbf{k}_s;\mathbf{k}_3,\mathbf{k}_2,\mathbf{k}_1,t_3,t_2,t_1)&=i\sum_{abcd}P(a)\int d\mathbf{r}\int d\mathbf{r}_3\int d\mathbf{r}_2\int d\mathbf{r}_1j_{ab}(\mathbf{r})j_{bc}(\mathbf{r}_3)j_{cd}(\mathbf{r}_2)j_{da}(\mathbf{r}_1)\\&\quad\times\exp[-i\mathbf{k}_3\cdot(\mathbf{r}-\mathbf{r}_3)-i\mathbf{k}_2\cdot(\mathbf{r}-\mathbf{r}_2)-i\mathbf{k}_1\cdot(\mathbf{r}-\mathbf{r}_1)]I_{ba}(t_3)I_{ca}(t_2)I_{da}(t_1),\end{aligned}\tag{A6d}$$

where a,b,c, and d denote the many-electron states and j_{ab} is the matrix element of the current-density operator between the states a and b. The thermal population for the state a, $P(a)$, is goverend by Boltzmann distribution function. $I_{ab}(t)$ is an auxiliary function representing the Liouville space Green function [16,20]

$$I_{ab}(t)\equiv\theta(t)\exp(-i\omega_{ab}-\Gamma_{ab}),\tag{A7}$$

where $\omega_{ab}=\epsilon_a-\epsilon_b$ is the transition frequency between states a and b.

We next apply this formula to the three band core-exciton model shown in Fig. 1(b). The ground, single-core-excited state, and valence-excited state are denoted by $|g\rangle$, $|e\rangle$ (or $|e'\rangle$), and $|g'\rangle$, respectively. When all the incoming x-ray beams are nearly resonant with the single-core-excitation energies, there are only seven Liouville space pathways which survive under RWA (rotating wave approximation), as shown in Fig. 13 in Ref. [18]. By expanding Eqs. (A6) in terms of

the eigenstates of H_{mat}, we then have

$$R_I(-\mathbf{k}_3+\mathbf{k}_2-\mathbf{k}_1;\mathbf{k}_3,-\mathbf{k}_2,\mathbf{k}_1,t_3,t_2,t_1) = i\sum_{gee'g'} P(g)J_{g'e;eg}(\mathbf{k}_3-\mathbf{k}_2)J^*_{g'e';e'g}(\mathbf{k}_3-\mathbf{k}_2) \times I_{eg'}(t_3)I_{ee'}(t_2)I_{eg}(t_1), \tag{A8a}$$

$$R_{II}(-\mathbf{k}_3-\mathbf{k}_2+\mathbf{k}_1;\mathbf{k}_3,\mathbf{k}_2,-\mathbf{k}_1,t_3,t_2,t_1) = i\sum_{gee'g'} P(g)J_{g'e;eg}(\mathbf{k}_3-\mathbf{k}_1)J^*_{g'e';e'g}(\mathbf{k}_3-\mathbf{k}_1) \times I_{eg'}(t_3)I_{ee'}(t_2)I_{ge'}(t_1), \tag{A8b}$$

$$R_{III}(-\mathbf{k}_3-\mathbf{k}_2+\mathbf{k}_1;\mathbf{k}_3,\mathbf{k}_2,-\mathbf{k}_1,t_3,t_2,t_1) = i\sum_{gee'g'} P(g)J_{g'e;eg}(\mathbf{k}_2-\mathbf{k}_1)J^*_{g'e';e'g}(\mathbf{k}_2-\mathbf{k}_1) \times I_{eg'}(t_3)I_{gg'}(t_2)I_{ge'}(t_1), \tag{A8c}$$

$$R_{IV}(-\mathbf{k}_3+\mathbf{k}_2-\mathbf{k}_1;\mathbf{k}_3,-\mathbf{k}_2,\mathbf{k}_1,t_3,t_2,t_1) = i\sum_{gee'g'} P(g)J_{ge';e'g'}(\mathbf{k}_1-\mathbf{k}_2)J^*_{ge;eg'}(\mathbf{k}_1-\mathbf{k}_2) \times I_{e'g}(t_3)I_{g'g}(t_2)I_{eg}(t_1), \tag{A8d}$$

$$R_V(-\mathbf{k}_3-\mathbf{k}_2+\mathbf{k}_1;\mathbf{k}_3,\mathbf{k}_2,-\mathbf{k}_1,t_3,t_2,t_1) = -i\sum_{gee'f} P(g)[J_{e'f;fe}(\mathbf{k}_1-\mathbf{k}_2)J_{eg;ge'}(\mathbf{k}_2-\mathbf{k}_1) + J_{fe;ge'}(\mathbf{k}_1-\mathbf{k}_3)J^*_{fe';ge}(\mathbf{k}_1-\mathbf{k}_3)] \times I_{fe'}(t_3)I_{ee'}(t_2)I_{ge'}(t_1), \tag{A8e}$$

$$R_{VI}(\mathbf{k}_3-\mathbf{k}_2-\mathbf{k}_1;-\mathbf{k}_3,\mathbf{k}_2,\mathbf{k}_1,t_3,t_2,t_1) = -i\sum_{gee'f} P(g)[J_{fe;e'f}(\mathbf{k}_1-\mathbf{k}_3)J_{eg;ge'}(\mathbf{k}_3-\mathbf{k}_1) + J_{eg;e'f}(\mathbf{k}_2-\mathbf{k}_3)J_{fe;ge'}(\mathbf{k}_3-\mathbf{k}_2)] \times I_{fe'}(t_3)I_{fg}(t_2)I_{eg}(t_1), \tag{A8f}$$

$$R_{VII}(-\mathbf{k}_3+\mathbf{k}_2-\mathbf{k}_1;\mathbf{k}_3,-\mathbf{k}_2,\mathbf{k}_1,t_3,t_2,t_1) = -i\sum_{gee'f} P(g)[J_{fe;e'f}(\mathbf{k}_1-\mathbf{k}_2)J_{eg;ge'}(\mathbf{k}_2-\mathbf{k}_1) + J_{fe;ge'}(\mathbf{k}_2-\mathbf{k}_3)J_{eg;e'f}(\mathbf{k}_3-\mathbf{k}_2)] \times I_{fe'}(t_3)I_{ee'}(t_2)I_{eg}(t_1). \tag{A8g}$$

The heterodyne TCXRS signal is given in Eq. (10). Combining Eqs. (10), (A2), (A4), and (A8), the signal is obtained by summing over all the contributions of the seven Liouville pathways

$$S_{TCXRS}(\mathbf{k}_s,\tau) = \sum_{j=I}^{VII} S_j(\mathbf{k}_s,\tau), \tag{A9}$$

where

$$S_I(\mathbf{k}_s,\tau) = \frac{-2}{\hbar^3}\frac{1}{\omega_3\omega_2\omega_1\omega_s}\mathrm{Im}\int_{-\infty}^{\infty}dt\int_0^{\infty}dt_3\int_0^{\infty}dt_2\int_0^{\infty}dt_1 R_I(-\mathbf{k}_s;\mathbf{k}_3,-\mathbf{k}_2,\mathbf{k}_1,t_3,t_2,t_1) \times \exp[i(\omega_3-\omega_2+\omega_1)t_3 - i(\omega_2-\omega_1)t_2 + i\omega_1 t_1]E^*_{LO}(t)E_3(t-t_3)E^*_2(t+\tau-t_3-t_2)E_1(t+\tau-t_3-t_2-t_1), \tag{A10a}$$

$$S_{II}(\mathbf{k}_s,\tau) = \frac{-2}{\hbar^3}\frac{1}{\omega_3\omega_2\omega_1\omega_s}\mathrm{Im}\int_{-\infty}^{\infty}dt\int_0^{\infty}dt_3\int_0^{\infty}dt_2\int_0^{\infty}dt_1 R_{II}(-\mathbf{k}_s;\mathbf{k}_3,\mathbf{k}_2,-\mathbf{k}_1,t_3,t_2,t_1) \times \exp[i(\omega_3+\omega_2-\omega_1)t_3 \quad + i(\omega_2-\omega_1)t_2 - i\omega_1 t_1]E^*_{LO}(t)E_3(t-t_3)E_2(t+\tau-t_3-t_2)E^*_1(t+\tau-t_3-t_2-t_1), \tag{A10b}$$

$$S_{III}(\mathbf{k}_s,\tau) = \frac{-2}{\hbar^3}\frac{1}{\omega_3\omega_2\omega_1\omega_s}\mathrm{Im}\int_{-\infty}^{\infty}dt\int_0^{\infty}dt_3\int_0^{\infty}dt_2\int_0^{\infty}dt_1 R_{III}(-\mathbf{k}_s;\mathbf{k}_3,\mathbf{k}_2,-\mathbf{k}_1,t_3,t_2,t_1) \times \exp[i(\omega_3+\omega_2-\omega_1)t_3 \quad + i(\omega_2-\omega_1)t_2 - i\omega_1 t_1]E^*_{LO}(t)E_3(t-t_3)E_2(t+\tau-t_3-t_2)E^*_1(t+\tau-t_3-t_2-t_1), \tag{A10c}$$

$$S_{IV}(\mathbf{k}_s,\tau) = \frac{-2}{\hbar^3}\frac{1}{\omega_3\omega_2\omega_1\omega_s}\mathrm{Im}\int_{-\infty}^{\infty}dt\int_0^{\infty}dt_3\int_0^{\infty}dt_2\int_0^{\infty}dt_1 R_{IV}(-\mathbf{k}_s;\mathbf{k}_3,-\mathbf{k}_2,\mathbf{k}_1,t_3,t_2,t_1) \times \exp[i(\omega_3-\omega_2+\omega_1)t_3 \quad - i(\omega_2-\omega_1)t_2 + i\omega_1 t_1]E^*_{LO}(t)E_3(t-t_3)E^*_2(t+\tau-t_3-t_2)E_1(t+\tau-t_3-t_2-t_1), \tag{A10d}$$

$$S_V(\mathbf{k}_s,\tau)=\frac{-2}{\hbar^3}\frac{1}{\omega_3\omega_2\omega_1\omega_s}\mathrm{Im}\int_{-\infty}^{\infty}dt\int_0^{\infty}dt_3\int_0^{\infty}dt_2\int_0^{\infty}dt_1 R_V(-\mathbf{k}_s;\mathbf{k}_3,\mathbf{k}_2,-\mathbf{k}_1,t_3,t_2,t_1)$$
$$\times\exp[i(\omega_3+\omega_2-\omega_1)t_3 \quad +i(\omega_2-\omega_1)t_2-i\omega_1 t_1]E^*_{LO}(t)E_3(t-t_3)E_2(t+\tau-t_3-t_2)E^*_1(t+\tau-t_3-t_2-t_1), \tag{A10e}$$

$$S_{VI}(\mathbf{k}_s,\tau)=\frac{-2}{\hbar^3}\frac{1}{\omega_3\omega_2\omega_1\omega_s}\mathrm{Im}\int_{-\infty}^{\infty}dt\int_0^{\infty}dt_3\int_0^{\infty}dt_2\int_0^{\infty}dt_1 R_{VI}(-\mathbf{k}_s;-\mathbf{k}_3,\mathbf{k}_2,\mathbf{k}_1,t_3,t_2,t_1)$$
$$\times\exp[-i(\omega_3-\omega_2-\omega_1)t_3 \quad +i(\omega_2+\omega_1)t_2+i\omega_1 t_1]E^*_{LO}(t)E^*_3(t-t_3)E_2(t+\tau-t_3-t_2)E_1(t+\tau-t_3-t_2-t_1), \tag{A10f}$$

$$S_{VII}(\mathbf{k}_s,\tau)=\frac{-2}{\hbar^3}\frac{1}{\omega_3\omega_2\omega_1\omega_s}\mathrm{Im}\int_{-\infty}^{\infty}dt\int_0^{\infty}dt_3\int_0^{\infty}dt_2\int_0^{\infty}dt_1 R_{VII}(-\mathbf{k}_s;\mathbf{k}_3,-\mathbf{k}_2,\mathbf{k}_1,t_3,t_2,t_1)$$
$$\times\exp[i(\omega_3-\omega_2+\omega_1)t_3 \quad -i(\omega_2-\omega_1)t_2+i\omega_1 t_1]E^*_{LO}(t)E_3(t-t_3)E^*_2(t+\tau-t_3-t_2)E_1(t+\tau-t_3-t_2-t_1). \tag{A10g}$$

Among all the Liouville space pathways (I)–(VII), S_V to S_{VII} which include the double-core-excited states, give a small contribution to the signal, because the double-core-excited state lifetimes are extremely short and they can only contribute within a very short-time period. Similarly S_I and S_{II} include the electronic population of the single-core-excited state during the time period t_2; these contributions are rather small compared to S_{III} and S_{IV}. Only S_{IV} survives under the phase-matching condition $\mathbf{k}_s=\mathbf{k}_3-\mathbf{k}_2+\mathbf{k}_1$.

APPENDIX B: DOORWAY-WINDOW EXPRESSION FOR TCXRS

To derive the doorway-window expression for TCXRS, we start with Eq. (11) and change the time variables to obtain

$$S_{IV}(\mathbf{k}_s;\tau)$$
$$=\frac{-2}{\hbar^3}\frac{1}{\omega_3\omega_2\omega_1\omega_s}\mathrm{Im}\int_{-\infty}^{\infty}dt\int_{-\infty}^{t}d\tau_3\int_{-\infty}^{\tau_3+\tau}d\tau_2$$
$$\times\int_{-\infty}^{\tau_2}d\tau_1 R_{IV}(-\mathbf{k}_s;\mathbf{k}_3,-\mathbf{k}_2,\mathbf{k}_1,t-\tau_3,\tau_3-\tau_2$$
$$+\tau,\tau_2-\tau_1)E^*_{LO}(t)E_3(\tau_3)E^*_2(\tau_2)E_1(\tau_1)$$
$$\times\exp[i(\omega_3-\omega_2+\omega_1)(t-\tau_3)-i(\omega_2-\omega_1)\tau_3$$
$$+i\omega_2\tau_2-i\omega_1\tau_1+i(\omega_2-\omega_1)\tau]. \tag{B1}$$

Assuming no temporal overlap between the first two pulses, $\mathbf{k}_1$ and $\mathbf{k}_2$, and the latter two pulses, $\mathbf{k}_3$ and $\mathbf{k}_{LO}$, we can safely extend the upper limit of the integral for τ_2 to infinity, which results in

$$S_{IV}(\mathbf{k}_s;\tau)$$
$$=\frac{-2}{\hbar^3}\frac{1}{\omega_3\omega_2\omega_1\omega_s}\mathrm{Re}\sum_{gee'g'}P(g)J_{ge';e'g'}(\mathbf{k}_1-\mathbf{k}_2)$$
$$\times J^*_{ge;eg'}(\mathbf{k}_1-\mathbf{k}_2)\int_{-\infty}^{\infty}dt\int_{-\infty}^{t}d\tau_3\int_{-\infty}^{\infty}d\tau_2\int_{-\infty}^{\tau_2}d\tau_1$$
$$\times E^*_{LO}(t)E_3(\tau_3)E^*_2(\tau_2)E_1(\tau_1)I_{e'g}(t-\tau_3)$$
$$\times I_{g'g}(\tau_3-\tau_2+\tau)I_{eg}(\tau_2-\tau_1)\exp[i(\omega_3-\omega_2$$
$$+\omega_1)t \quad -i\omega\tau_3+i\omega_2\tau_2-i\omega_1\tau_1+i(\omega_2-\omega_1)\tau], \tag{B2}$$

or

$$S_{IV}(\mathbf{k}_s;\tau)$$
$$=\frac{-2}{\hbar^3}\frac{1}{\omega_3\omega_2\omega_1\omega_s}\mathrm{Re}\sum_{gee'g'}P(g)J_{ge';e'g'}(\mathbf{k}_1-\mathbf{k}_2)$$
$$\times J^*_{ge;eg'}(\mathbf{k}_1-\mathbf{k}_2)\exp[i(\omega_1-\omega_2)\tau]\int_{-\infty}^{\infty}dt\int_0^{\infty}dt_3$$
$$\times\exp[-i(\omega_2-\omega_1)t+i(\omega_3-\omega_2+\omega_1)t_3]$$
$$\times E^*_{LO}(t+t_3)E_3(t)\int_{-\infty}^{\infty}dt'\int_0^{\infty}dt_1$$
$$\times\exp[i\omega_2 t'-i\omega_1(t'-t_1)]E^*_2(t')E_1(t'-t_1)$$
$$\times I_{e'g}(t_3)I_{g'g}(t)I_{g'g}(\tau)I_{g'g}(-t_1)I_{eg}(t_1). \tag{B3}$$

Using the definition of the doorway and the window functions [Eqs. (14) and (15), Eq. (B3)] finally leads to Eq. (13).

APPENDIX C: THE DOORWAY FUNCTION IN THE SNAPSHOT LIMIT

In this appendix we prove that in the snapshot limit the time evolution of the TCXRS coincides with that of the reduced density operator defined in Eq. (21).

In terms of the density operator defined in Eq. (20) the doorway-window expression for the TCXRS Eq. (13) can be recast in the form

$$\begin{aligned} S_{\mathrm{TCXRS}}(\mathbf{k}_s;\tau) &= \frac{2}{\hbar}\mathrm{Re}\sum_{g'} W_{gg'}(\omega_1,\omega_2,\omega_3) \\ &\quad \times \mathrm{Tr}[|g\rangle\langle g'|\rho_{IV}(\omega_1,\omega_2;\tau)] \\ &= \frac{2}{\hbar}\mathrm{Re}\sum_{g'} W_{gg'}(\omega_1,\omega_2,\omega_3) \\ &\quad \times \langle g'|\rho_{IV}(\omega_1,\omega_2;\tau)|g\rangle. \end{aligned} \tag{C1}$$

We now assume that $\omega_s=\omega_3-\omega_2+\omega_1$ is near resonant with the core excitation of site b. In this case, the contribution of the core-excited state of site a has been averaged out by the t_3 integral of $W_{gg'}$

$$\begin{aligned} &\int_{-\infty}^{\infty} dt \int_0^{\infty} dt_3 E_{LO}^*(t+t_3)E_3(t) \\ &\quad \times \exp[-i\{\omega_{eg}-(\omega_3-\omega_2+\omega_1)\}t_3-\Gamma t_3] \\ &\quad \times \exp[-i\{\omega_{g'g}-(\omega_1-\omega_2)\}t-\gamma t], \end{aligned} \tag{C2}$$

because the phase of $\omega_{e_a g}-(\omega_3-\omega_2+\omega_1)$ changes rapidly during δ_2. On the other hand, the phase of $\omega_{e_b g}-(\omega_3-\omega_2+\omega_1)$ is slowly varying during δ_2 of the t_3 integral, so that we can take the following *snapshot limit*:

$$E_{LO}^*(t+t_3)E_3(t) \sim E_{LO}^*(t)E_3(t) \tag{C3}$$

leaving only e_b states in the summation of the core-excited states of $W_{g'g}$. We then have

$$\begin{aligned} &W_{gg'}(\omega_1,\omega_2,\omega_3) \\ &\simeq \frac{i\delta_2}{\hbar}\sum_{e=e_b} J_{ge;eg'}(\mathbf{q})\int_{-\infty}^{\infty} dt E_{LO}^*(t)E_3(t) \\ &\quad \times \exp[-i\{\omega_{g'g}-(\omega_1-\omega_2)\}t-\gamma t]. \end{aligned} \tag{C4}$$

Using the completeness relation

$$\sum_{e=e_b} J_{ge;eg'}(\mathbf{q}) = \exp[i\mathbf{q}\cdot(\mathbf{R}_1-\mathbf{R}_N)]\mu_N^{vc}\sum_{\sigma}\langle g|c_{N\sigma}v_{N\sigma}^{\dagger}|g'\rangle, \tag{C5}$$

Eq. (C4) is reduced to

$$\begin{aligned} &W_{gg'}(\omega_1,\omega_2,\omega_3) \\ &= \frac{i\delta_2}{\hbar}\exp[i\mathbf{q}\cdot(\mathbf{R}_1-\mathbf{R}_N)]\mu_N^{vc}\sum_{\sigma}\langle g|c_{N\sigma}v_{N\sigma}^{\dagger}|g'\rangle\int_{-\infty}^{\infty} dt \\ &\quad \times E_{LO}^*(t)E_3(t)\exp[-i\{\omega_{g'g}-(\omega_1-\omega_2)\}t-\gamma t]. \end{aligned} \tag{C6}$$

When δ_2 is shorter than the characteristic time scale of the valence-exciton wave-packet motion, we can assume

$$E_{LO}^*(t)E_3(t) \sim \delta(t), \tag{C7}$$

leading to

$$\begin{aligned} &W_{gg'}(\omega_1,\omega_2,\omega_3) \\ &= \frac{i\delta_2}{\hbar}\exp[i\mathbf{q}\cdot(\mathbf{R}_1-\mathbf{R}_N)]\mu_N^{vc}\sum_{\sigma}\langle g|c_{N\sigma}v_{N\sigma}^{\dagger}|g'\rangle. \end{aligned} \tag{C8}$$

Inserting this into Eq. (13) and comparing with Eqs. (20) and (21), we finally obtain

$$S_{\mathrm{TCXRS}}(\mathbf{k}_s;\tau) \propto -\mathrm{Re}[\rho_{IV;NN}(\tau)]. \tag{C9}$$

[1] A. Rousse, C. Rischel, and J.-G. Gauthier, Rev. Mod. Phys. **73**, 17 (2001).

[2] M. Hentschel, R. Klenberger, Ch. Spielmann, G.A. Reider, N. Milosevic, T. Brabec, P. Corkum, U. Helnzmann, M. Drescher, and F. Krausz, Nature (London) **414**, 519 (2001).

[3] R.W. Schoenlein, S. Chattopadhyay, H.H.W. Chong, T.E. Glover, P.A. Heimann, C.V. Shank, A.A. Zholents, and M.S. Zolotorev, Science **287**, 2237 (2000).

[4] A.H. Chin, R.W. Sconenlein, T.E. Glover, P. Balling, W.P. Leemans, and C.V. Shank, Phys. Rev. Lett. **83**, 336 (1999).

[5] M. Drescher, M. Hentshel, R. Kienberger, G. Tempea, C. Speilmann, G.A. Reider, P.B. Corkum, and F. Krausz, Science **291**, 1923 (2001).

[6] Y. Silberberg, Nature (London) **414**, 494 (2001).

[7] P.M. Rentzepis and J. Helliwell, *Time-Resolved Electron and X-ray Diffraction* (Oxford University Press, New York, 1995).

[8] K. Sokolowski-Tinten, C. Blome, C. Dietrich, A. Tarasevitch, M. Horn von Hoegen, D. von der Linde, A. Cavalleri, J. Squier, and M. Kammler, Phys. Rev. Lett. **87**, 225701 (2001).

[9] L.X. Chen, W.J.H. Jäger, G. Jennings, D.J. Gosztola, A. Munkholm, and J.P. Hessler, Science **292**, 262 (2001).

[10] C. Bressler, M. Saes, M. Chegui, D. Grolimund, R. Abela, and P. Pattison, J. Chem. Phys. **116**, 2955 (2002).

[11] M. Ben-Nun, J. Cao, and K. Wilson, J. Phys. Chem. A **101**, 8743 (1997).

[12] J. Cao and K.R. Wilson, J. Phys. Chem. **102**, 9523 (1998).

[13] Y. Ma, K.E. Miyano, P.L. Cowan, Y. Aglitzkiy, and B.A. Karlin, Phys. Rev. Lett. **74**, 478 (1995).

[14] S.F. Parker, D.A. Braden, J. Tomkinson, and B.S. Hudson, J. Phys. Chem. B **102**, 5955 (1998).

[15] S. Tanaka, V. Chernyak, and S. Mukamel, Phys. Rev. A **63**, 063405 (2001).

[16] S. Mukamel, *Principles of Nonlinear Optical Spectroscopy* (Oxford, New York, 1995).
[17] S. Bratos, F. Mirloup, R. Vuilleumier, and M. Wulff, J. Chem. Phys. **116**, 10 615 (2002).
[18] S. Tanaka and S. Mukamel, J. Chem. Phys. **116**, 1877 (2002).
[19] S. Tanaka and S. Mukamel, Phys. Rev. Lett. **89**, 043001 (2002).
[20] S. Tanaka and S. Mukamel, Phys. Rev. A **64**, 032503 (2001).
[21] S. Tanaka and S. Mukamel, in *Ultrafast Phenomena XIII*, edited by N. Scherer, M. Murnane, R. Miller, and A. Wiersma (Springer-Verlag, Berlin, 2002).
[22] *Light Scattering in Solids*, edited by M. Cardona and G. Güntherodt (Springer, New York, 2000), Vol. VIII.
[23] The acronyms CARS (coherent antistokes Raman scattering) and CSRS (coherent Stokes Raman scattering) are normally used for $\omega_1 > \omega_2 (\omega_1 < \omega_2)$, respectively. However, we shall avoid this historical distinction since it has no fundamental significance, and simply denote both as CRS.
[24] S. Tanaka and A. Kotani, J. Phys. Soc. Jpn. **62**, 464 (1993).
[25] S. Tanaka and Y. Kayanuma, Solid State Commun. **64**, 77 (1996).
[26] F. Gel'mukhanov and H. Ågren, Phys. Rep. **312**, 87 (1999).
[27] J.-E. Rubensson, J. Electron Spectrosc. Relat. Phenom. **110-111**, 135 (2000).
[28] A. Kotani and S. Shin, Rev. Mod. Phys. **73**, 203 (2001).
[29] *Relaxation in Polymers*, edited by T. Kobayashi (World Scientific, Singapore, 1993).
[30] S. Tretiak and S. Mukamel, Chem. Rev. **102**, 3171 (2002).
[31] S.L. Dexheimer, A.D. Van Pelt, J.A. Brozik, and B.I. Swanson, Phys. Rev. Lett. **84**, 4425 (2000).
[32] B.I. Swanson, J.A. Brozik, S.P. Love, G.F. Strouse, A.P. Shreve, A.R. Bishop, W.-Z. Wang, and M.I. Salkola, Phys. Rev. Lett. **82**, 3288 (1999).
[33] S. Tomimoto, S. Saito, T. Suemoto, K. Sakata, J. Takeda, and S. Kurita, Phys. Rev. B **60**, 7961 (1999).
[34] The transfer integrals of a core orbit are usually very small. Those values were estimated ~ 0.1 eV in C $1s$ orbital in C_2H_2, which is considered to have a large transfer integral of the core orbitals. See, for example, B. Kempgens, H. Köppel, A. Kivimäki, M. Neeb, L.S. Cederbaum, and A.M. Bradshaw, Phys. Rev. Lett. **79**, 3617 (1997).
[35] Y.J. Yan and S. Mukamel, Phys. Rev. A **41**, 6485 (1990).
[36] M.S. Deleuze and L.S. Cederbaum, Adv. Quantum Chem. **35**, 77 (1999).
[37] N.V. Dobrodey, A.I. Streltsov, and L.S. Cederbaum, Phys. Rev. A **65**, 023203 (2002).
[38] S. Mukamel, S. Tretiak, T. Wagersreiter, and V. Chernyak, Science **277**, 781 (1997).
[39] T.S. Rose, R. Righini, and M.D. Fayer, Chem. Phys. Lett. **106**, 13 (1984).
[40] J. Knoester and S. Mukamel, Phys. Rep. **205**, 1 (1991).
[41] G. J. Small, in *Excited States*, edited by E.C. Lim (Academic Press, New York, 1982).
[42] H. Haug and S. W. Koch, *Quantum Theory of the Optical Electronic Properties of Semiconductors*, 3rd ed. (World Scientific, Singapore, 1994).
[43] D.S. Chemla and J. Shah, Nature (London) **411**, 549 (2001).
[44] S. Schmitt-Rink, S. Mukamel, K. Leo, J. Shah, and D.S. Chemla, Phys. Rev. A **44**, 2124 (1991).
[45] N.H. Bonadeo, J. Erland, D. Gammon, D. Park, D.S. Katzer, and D.G. Steel, Science **282**, 1473 (1998).
[46] M. Drescher, M. Hentschel, R. Kienberger, M. Uiberacker, V. Yakovlev, A. Scrinzi, Th. Westerwalbesloh, U. Kleineberg, U. Heinzmann, and F. Krausz, Nature (London) **419**, 803 (2002).
[47] *Nonlinear Optics of Organics and Semiconductors*, edited by T. Kobayashi, Springer Proceedings in Physics Vol. 36 (Springer-Verlag, Berlin, 1989).
[48] R. Bartels *et al*., in *Ultrafast Phenomena XIII*, edited by R.J. Miller, M.M. Murnane, N.F. Scherer, and A.M. Wiener (Springer-Verlag, Berlin, 2002).
[49] L. Campbell, L. Hedin, J.J. Rehr, and W. Bardyszewski, Phys. Rev. B **65**, 064107 (2002).
[50] T. Fujikawa, J. Phys. Soc. Jpn. **62**, 2155 (1993).
[51] W. Bardyszewski and L. Hedin, Phys. Scr. **32**, 439 (1985).
[52] J.E. Inglesfield, J. Phys. C **16**, 403 (1983).